Supporting Information: Twist Angle-Dependent Atomic Reconstruction and Moiré Patterns in Transition Metal Dichalcogenide Heterostructures

*Matthew R. Rosenberger,[*1&] Hsun-Jen Chuang,[*%1] Madeleine Phillips,[#1] Vladimir P. Oleshko,[2] Kathleen M. McCreary,[1] Saujan V. Sivaram,[$1] C. Stephen Hellberg,[1] and Berend T. Jonker[1]*

[*] These authors contributed equally to this work.

[1] U.S. Naval Research Laboratory, Washington, DC 20375, USA

[2] National Institute of Standards and Technology, Gaithersburg, MD 20899, USA

[#] National Research Council Postdoctoral Fellow

[$] Former National Research Council Postdoctoral Fellow

[%] American Society of Engineering Education Postdoctoral Fellow

[&] Corresponding Author Email: matthew.rosenberger.ctr@nrl.navy.mil

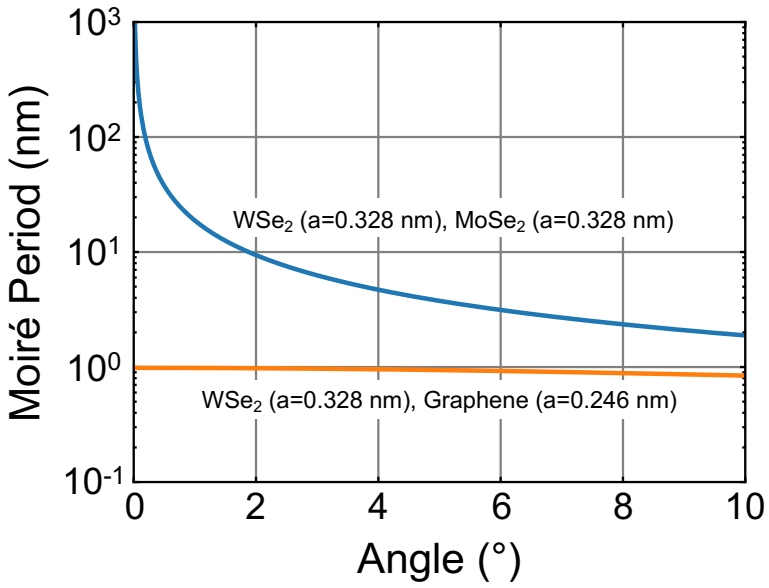

Figure S1. Moiré period as a function of twist angle for a $MoSe_2/WSe_2$ heterostructure and a WSe_2/graphene heterostructure. The lattice constant is assumed to be 0.328 nm, 0.328 nm, and 0.246 nm for $MoSe_2$, WSe_2, and graphene, respectively. The moiré period for lattice-matched materials is a strong function of angle, particularly near 0°, while the moiré period for materials with a large lattice mismatch is a very weak function of angle.

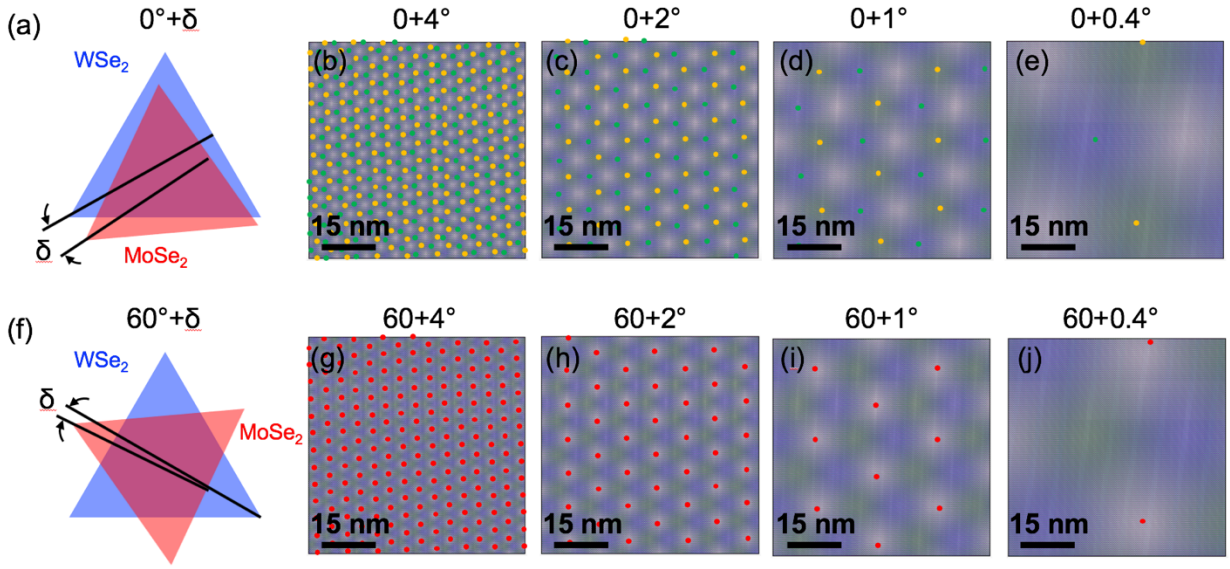

Figure S2. Rigid-lattice moiré patterns of atomic lattices of $MoSe_2$ and WSe_2 with different angular alignment showing a similar pattern for all δ, but with a larger period for smaller δ. (a) Diagram of the 0°+δ structure. (b-e) Patterns for the 0°+δ structure with different δ. The AB (green) and BA (gold) high symmetry, low stacking energy points are labeled in each image. (f) Diagram of the 60°+δ structure. (g-j) Patterns for the 60°+δ structure with different δ. The ABBA (red) high symmetry, low stacking energy points are labeled in each image. Importantly, for the rigid-lattice moiré pattern, the high symmetry, low energy stacking arrangements only occur at discrete points. In contrast, our experiments for structures with $\delta \leq 1°$ show large domains of constant stacking arrangement, which cannot be explained by a rigid-lattice moiré pattern.

Table S1. Summary of stacking arrangement nomenclature for TMD vdWH.

Authors	60°			0°		
Phillips, et al[1]	ABBA	AA	BB	AB	BA	AABB
Tong, et al[2]	H^{M}_{X}	H^{M}_{M}	H^{X}_{X}	R^{M}_{X}	R^{X}_{M}	R^{M}_{M}
Naik, et al[3]	AB	$B^{M/M}$	$B^{X/X}$	$B^{M/X}$	$B^{X/M}$	AA
Yu, et al[4]				R^{X}_{h}	R^{M}_{h}	R^{h}_{h}
Tran, et al[5]						
Wu, et al[6]	AB			AA		
Hsu, et al[7]						
Terrones, et al[8]	B	AB2			AB1	A
Rivera, et al[9]				R^{X}_{h}	R^{M}_{h}	R^{h}_{h}
				AB_{Se}	AB_{W}	AA
Puretzky, et al[10]	2H	AB'	A'B			
Zhao, et al[11]		AA'			AB	
	2H	3R'	3R''	3R	3R*	2H'
	AA'	AB'	AC'	AB	BA	AA
Hu, et al[12]	AA'	AB'	A'B		AB	AA
Wu, et al[13]				$r_{0,1}$	$r_{0,2}$	$r_{0,0}$

(1) Phillips, M.; Hellberg, C. S. Commensurate Structures in Twisted Transition Metal Dichalcogenide Heterobilayers. **2019**, arXiv: 1909.02495. *ArXiv Cond-Mat*. https://arxiv.org/abs/1909.02495 (accessed September 12, 2019).

(2) Tong, Q.; Yu, H.; Zhu, Q.; Wang, Y.; Xu, X.; Yao, W. Topological Mosaics in Moiré Superlattices of van der Waals Heterobilayers. *Nat. Phys.* **2017**, *13*, 356–362.

(3) Naik, M. H.; Maity, I.; Maiti, P. K.; Jain, M. Kolmogorov–Crespi Potential for Multilayer Transition-Metal Dichalcogenides: Capturing Structural Transformations in Moiré Superlattices. *J. Phys. Chem. C* **2019**, *123*, 9770–9778.

(4) Yu, H.; Liu, G.-B.; Tang, J.; Xu, X.; Yao, W. Moiré Excitons: From Programmable Quantum Emitter Arrays to Spin-Orbit–Coupled Artificial Lattices. *Sci. Adv.* **2017**, *3*, e1701696.

(5) Tran, K.; Moody, G.; Wu, F.; Lu, X.; Choi, J.; Kim, K.; Rai, A.; Sanchez, D. A.; Quan, J.; Singh, A.; Embley, J.; Zepeda, A.; Campbell, M.; Autry, T.; Taniguchi, T.; Watanabe, K.; Lu, N.; Banerjee, S. K.; Silverman, K. L.; Kim, S.; Tutuc, E.; Yang, L.; MacDonald, A. H.; Li, X. Evidence for Moiré Excitons in van der Waals Heterostructures. *Nature* **2019**, *567*, 71–75.

(6) Wu, F.; Lovorn, T.; MacDonald, A. H. Topological Exciton Bands in Moiré Heterojunctions. *Phys. Rev. Lett.* **2017**, *118*, 147401.

(7) Hsu, W.-T.; Lu, L.-S.; Wu, P.-H.; Lee, M.-H.; Chen, P.-J.; Wu, P.-Y.; Chou, Y.-C.; Jeng, H.-T.; Li, L.-J.; Chu, M.-W.; Chang, W.-H. Negative Circular Polarization Emissions from $WSe_2/MoSe_2$ Commensurate Heterobilayers. *Nat. Commun.* **2018**, *9*, 1356.

(8) Terrones, H.; Terrones, M. Bilayers of Transition Metal Dichalcogenides: Different Stackings and Heterostructures. *J. Mater. Res.* **2014**, *29*, 373–382.

(9) Rivera, P.; Yu, H.; Seyler, K. L.; Wilson, N. P.; Yao, W.; Xu, X. Interlayer Valley Excitons in Heterobilayers of Transition Metal Dichalcogenides. *Nat. Nanotechnol.* **2018**, *13*, 1004–1015.

(10) Puretzky, A. A.; Liang, L.; Li, X.; Xiao, K.; Sumpter, B. G.; Meunier, V.; Geohegan, D. B. Twisted $MoSe_2$ Bilayers with Variable Local Stacking and Interlayer Coupling Revealed by Low-Frequency Raman Spectroscopy. *ACS Nano* **2016**, *10*, 2736–2744.

(11) Zhao, X.; Ding, Z.; Chen, J.; Dan, J.; Poh, S. M.; Fu, W.; Pennycook, S. J.; Zhou, W.; Loh, K. P. Strain Modulation by van der Waals Coupling in Bilayer Transition Metal Dichalcogenide. *ACS Nano* **2018**, *12*, 1940–1948.

(12) Hu, X.; Kou, L.; Sun, L. Stacking Orders Induced Direct Band Gap in Bilayer $MoSe_2$-WSe_2 Lateral Heterostructures. *Sci. Rep.* **2016**, *6*, 31122.

(13) Wu, F.; Lovorn, T.; MacDonald, A. H. Theory of Optical Absorption by Interlayer Excitons in Transition Metal Dichalcogenide Heterobilayers. *Phys. Rev. B* **2018**, *97*, 035306.

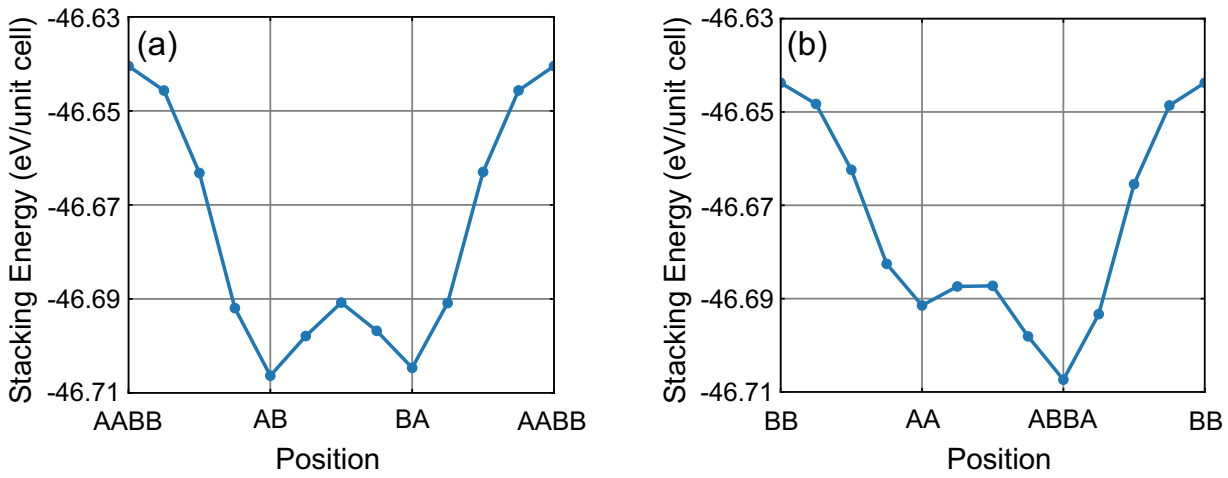

Figure S3. Interlayer stacking energy calculations for MoS_2/WS_2 structures for (a) 0° orientation and (b) 60° orientation. The results are qualitatively similar to the results for $MoSe_2/WSe_2$ structures.

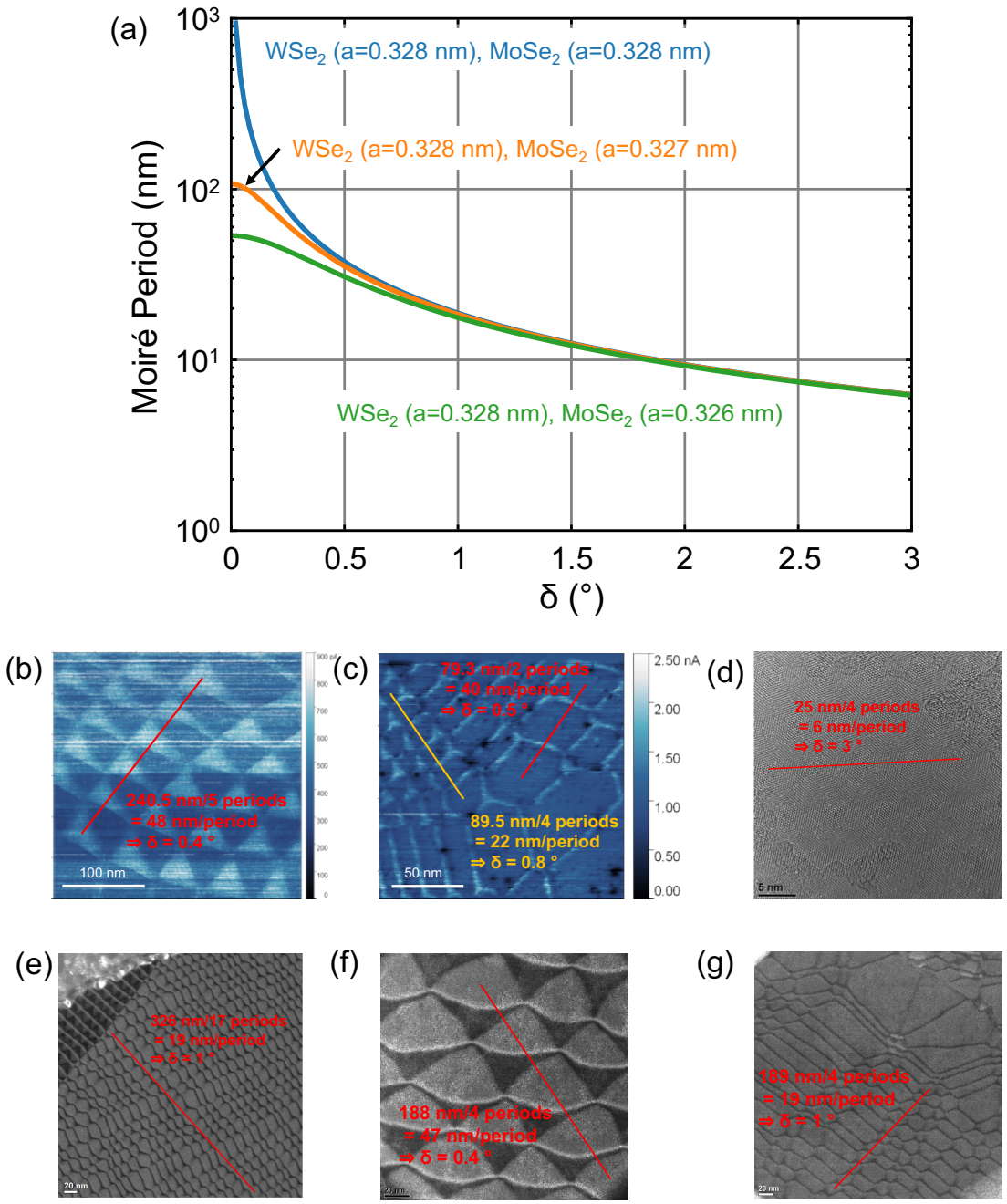

Figure S4. Estimation of local twist angle from the period of patterns observed with CAFM or TEM. (a) Moiré period as a function of misalignment angle, δ, for $MoSe_2/WSe_2$. The blue curve shows the moiré period assuming the lattice constants of $MoSe_2$ and WSe_2 are identical. The orange and green curves show the moiré period assuming a slight mismatch in lattice constant between the layers. (b-g) Estimated angles for: (b) Fig. 1(c), (c) Fig. 1(f), (d) Sample 1 in Fig. 2, (e) Sample 2 in Fig. 3, and (f-g) Sample 3 in Fig. 3. For the reported twist angles, we assumed that the lattice constant of both $MoSe_2$ and WSe_2 were 0.328 nm (blue curve in (a)). From (a), this assumption could lead to an overestimation of angle, particularly for small angles, if the lattice constants of $MoSe_2$ and WSe_2 are not exactly equal.

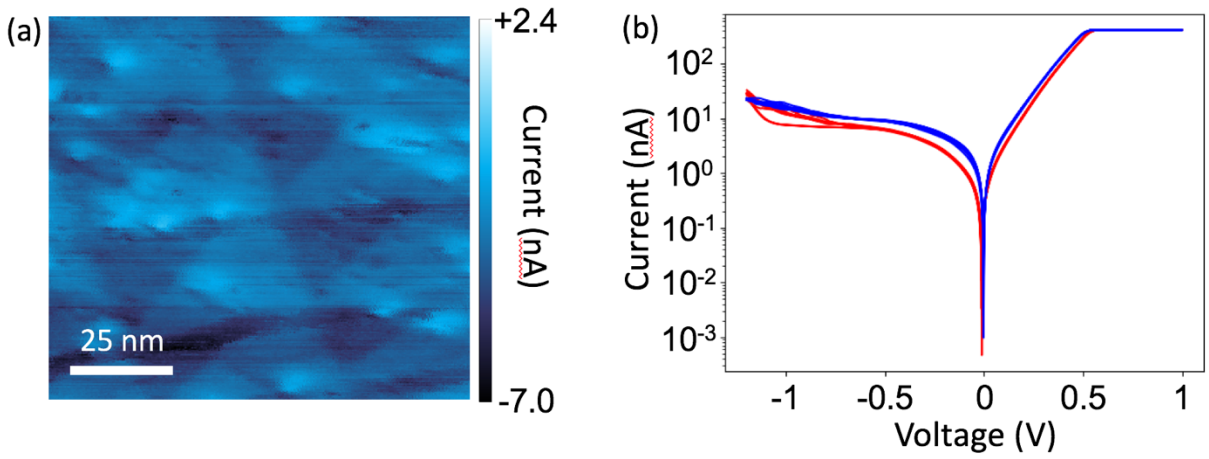

Figure S5. Observations of triangular reconstruction pattern in 0°+δ MoS_2/WS_2 heterostructures. (a) Conductive AFM image showing triangular domains of alternating conductivity. (b) IV curves on high conductivity (blue) and low conductivity (red) triangles.

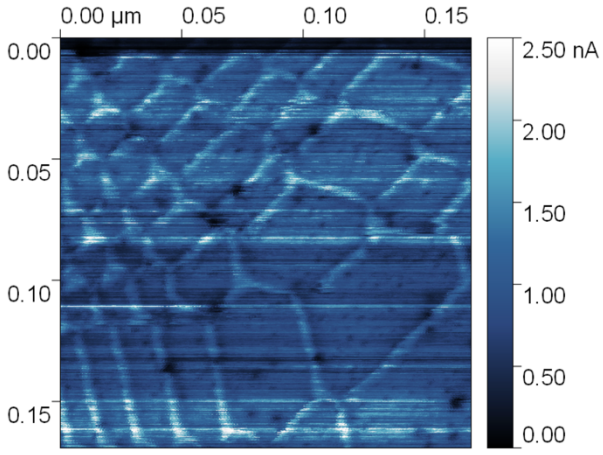

Figure S6. Raw data for Fig. 1(f).

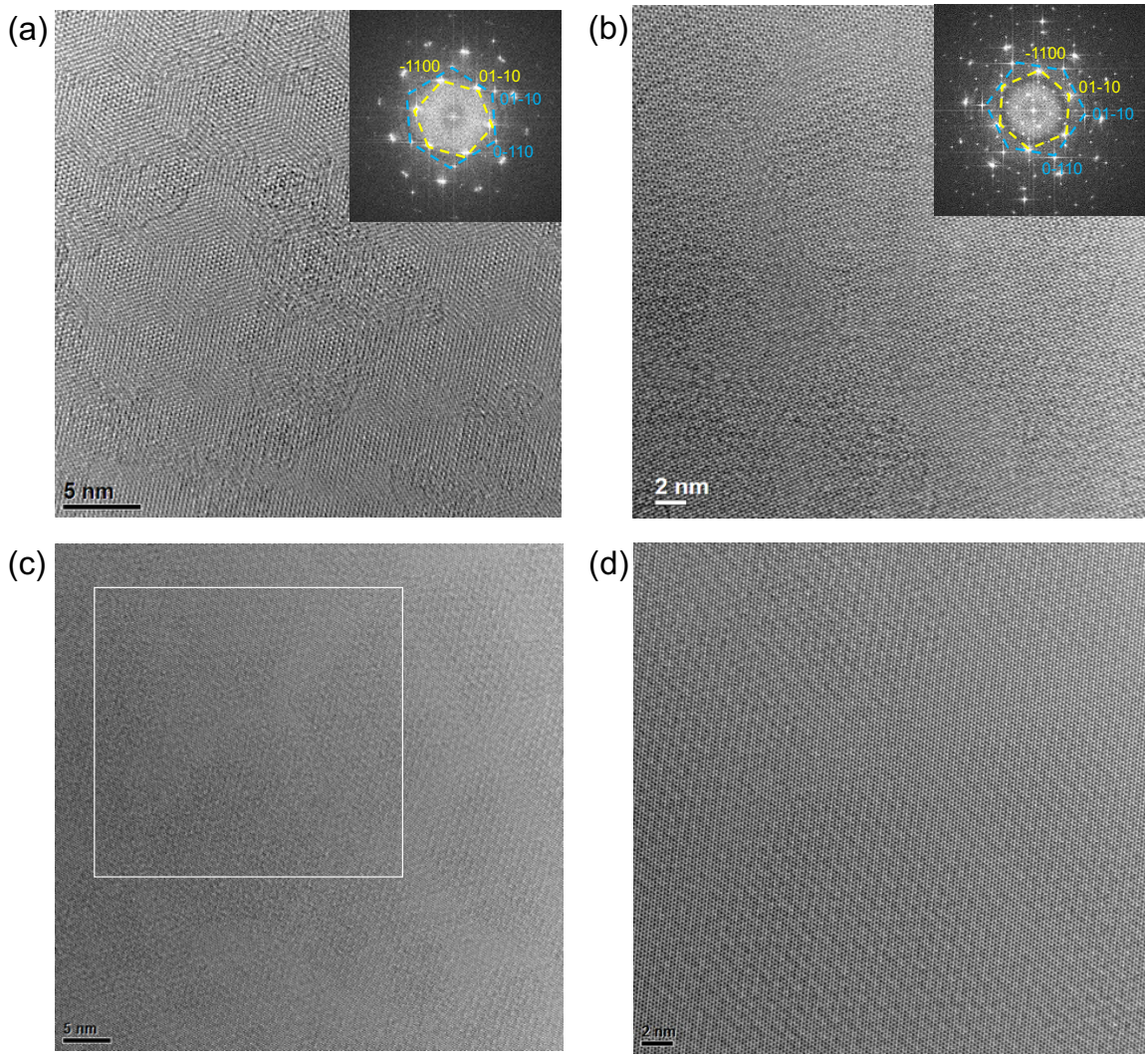

Figure S7. (a) HRTEM, a non-reconstructed hBN/$MoSe_2$/WSe_2 structure displaying a simple rigid-lattice moiré pattern and its Fast Fourier transform (FFT) pattern (inset), [0001] zone axis. Partially split larger $MoSe_2$ and WSe_2 point reflections are marked in yellow, and weaker h-BN point reflections are marked in blue. Note: no extra reflections observed in between the major Bragg reflections. (b) HRTEM, a reconstructed hBN/$MoSe_2$/WSe_2 and its FFT pattern (inset), [0001] zone axis. Larger $MoSe_2$ and WSe_2 point reflections are marked in yellow, and weaker hBN point reflections are marked in blue. Note: numerous extra reflections arise in between the major Bragg reflections. (c) HRTEM, a reconstructed 60^{o}+δ hBN/$MoSe_2$/WSe_2 from Figs. 2h and 2i showing hexagon-like domains and boundaries between them. (d) An enlarged view from the area marked by rectangular box in image (c) displaying periodic structural modulations within the domains likely induced by strain.

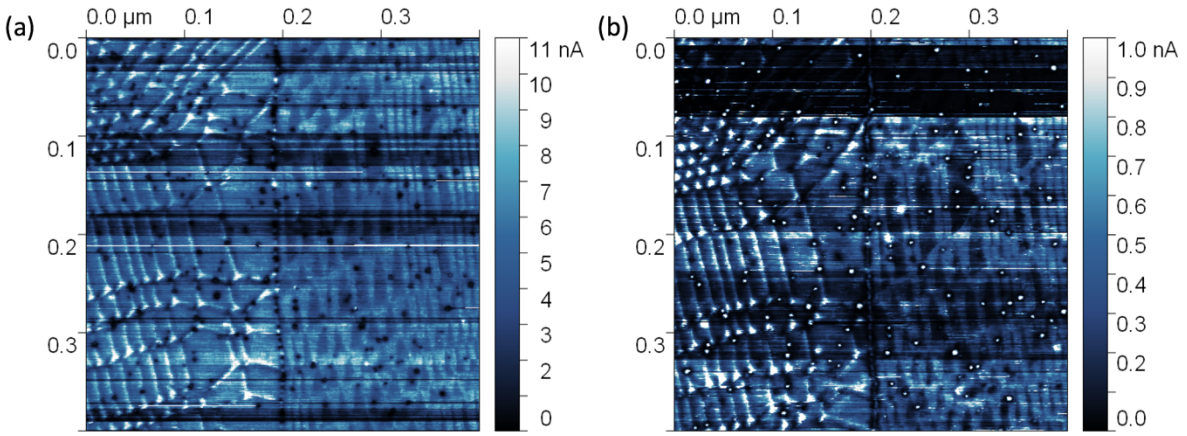

Figure S8. (a) Raw data for Fig. 4(a). Raw data for Fig. 4(b).

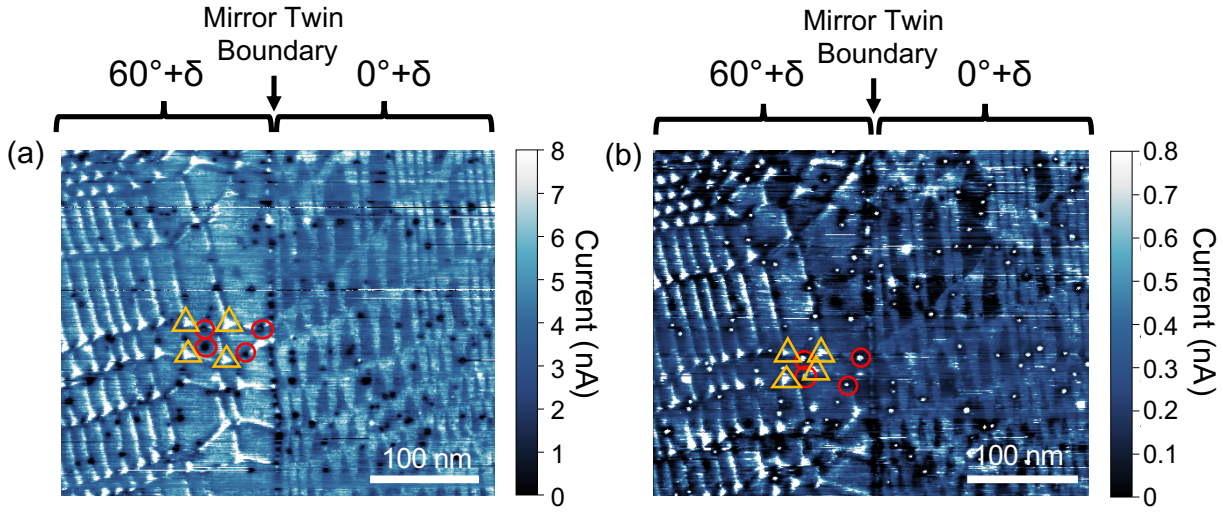

Figure S9. Evidence of domain boundary motion in reconstructed heterostructures. (a) CAFM scan of a reconstructed $MoSe_2/WSe_2$ structure. (b) CAFM scan of the same area taken at a later time. The red circles show what are believed to be point defects in either the $MoSe_2$ or WSe_2 layer which are assumed to not move between scans. The orange triangles mark four features from the reconstruction pattern. Comparing the location of the orange triangles with the red circles, there is clearly some motion of the reconstructed domain walls between/during CAFM scans.

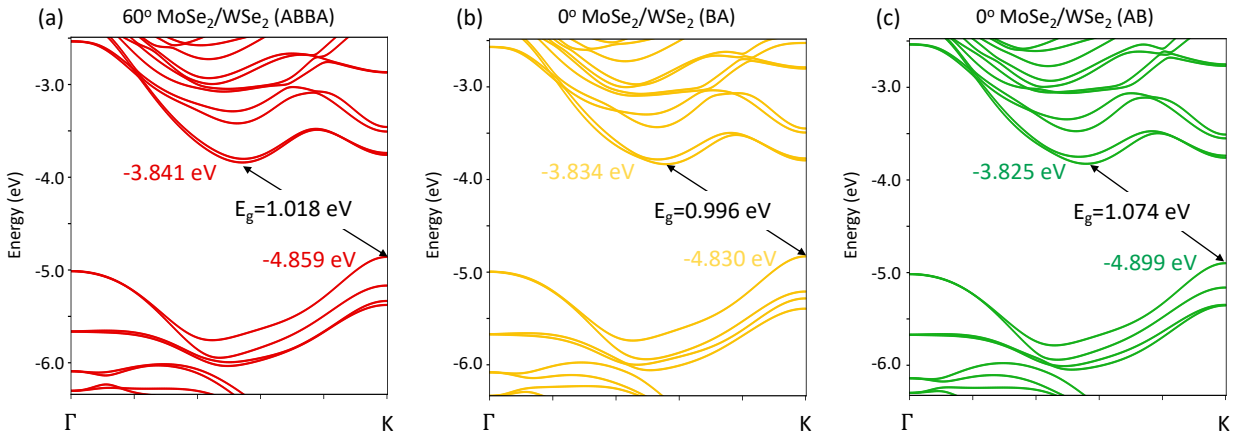

Figure S10. Vacuum-aligned DFT band structures with spin-orbit coupling for (a) the 60° ABBA stacked bilayer, (b) the 0° BA stacked bilayer, and (c) the 0° AB stacked bilayer. In all three bilayers, the band gap is indirect from K in the valence band to Q in the conduction band, where Q is a point lying between Γ and K. The smallest gap is in the 0° BA structure, and the largest gap is in the 0° AB structure. For details of the DFT calculations, see the Methods section.

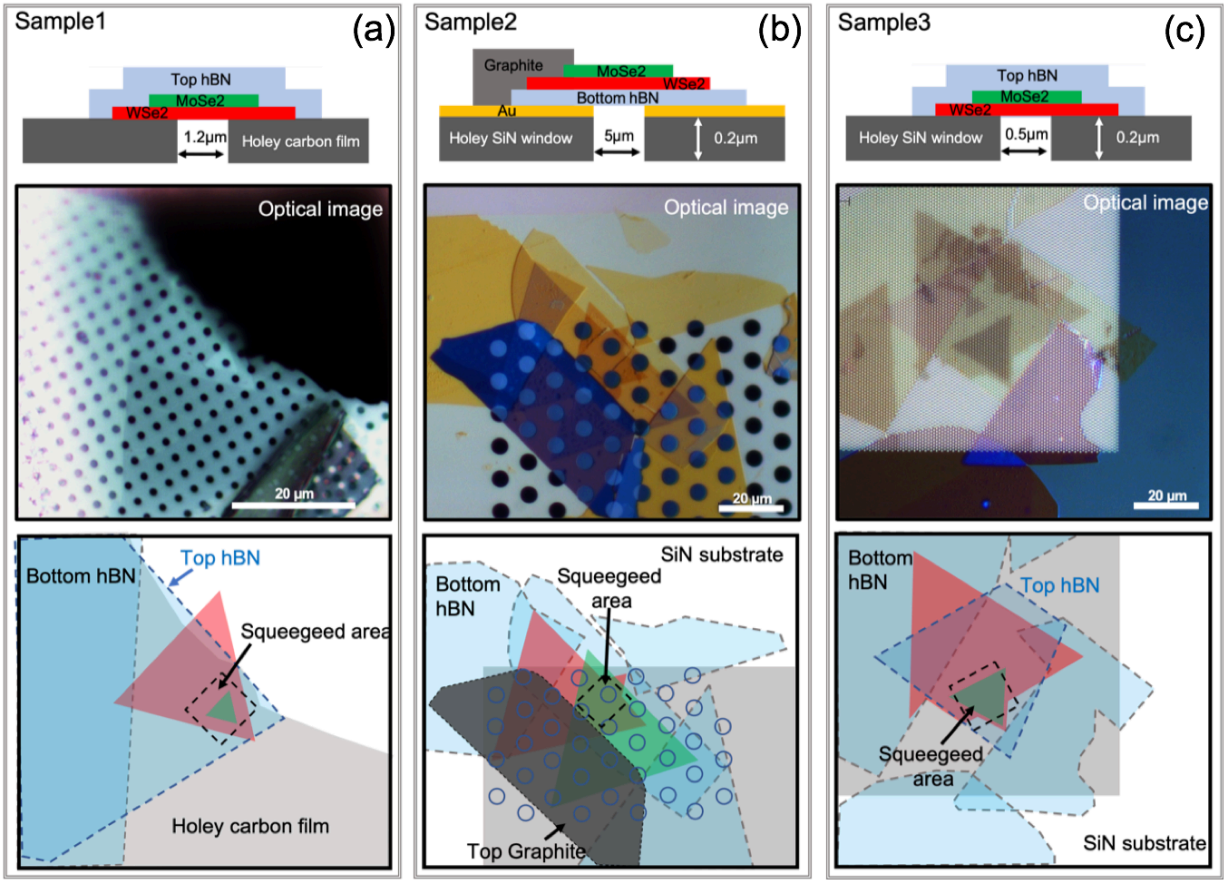

Figure S11. Sample diagrams and optical microscope images of TEM samples. (a) Sample 1 from Fig. 2. (b) Sample 2 from Fig. 3. (c) Sample 3 from Fig. 3.

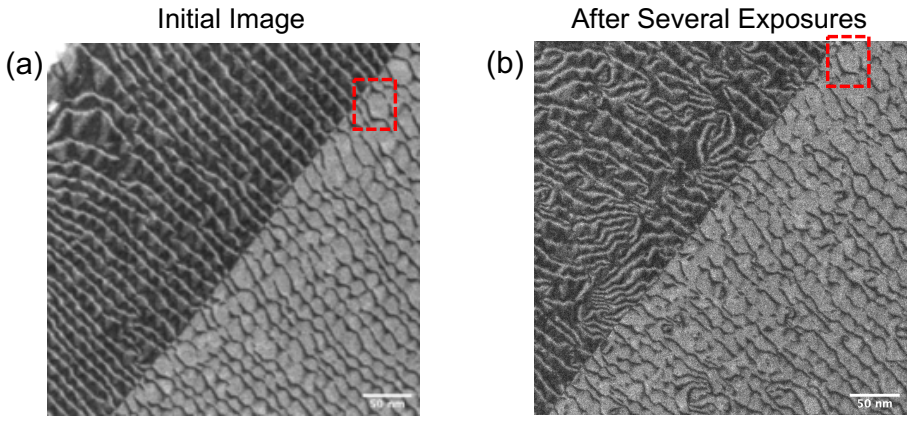

Figure S12. Evidence of damage from prolonged TEM exposure. (a) Initial dark-field TEM image of a reconstructed region similar to the region shown in Fig. 3(c). (b) Dark field TEM image of the same region after multiple repeated exposures of the same location. The dash red box shows a common feature in both both images to aid comparison of the images.

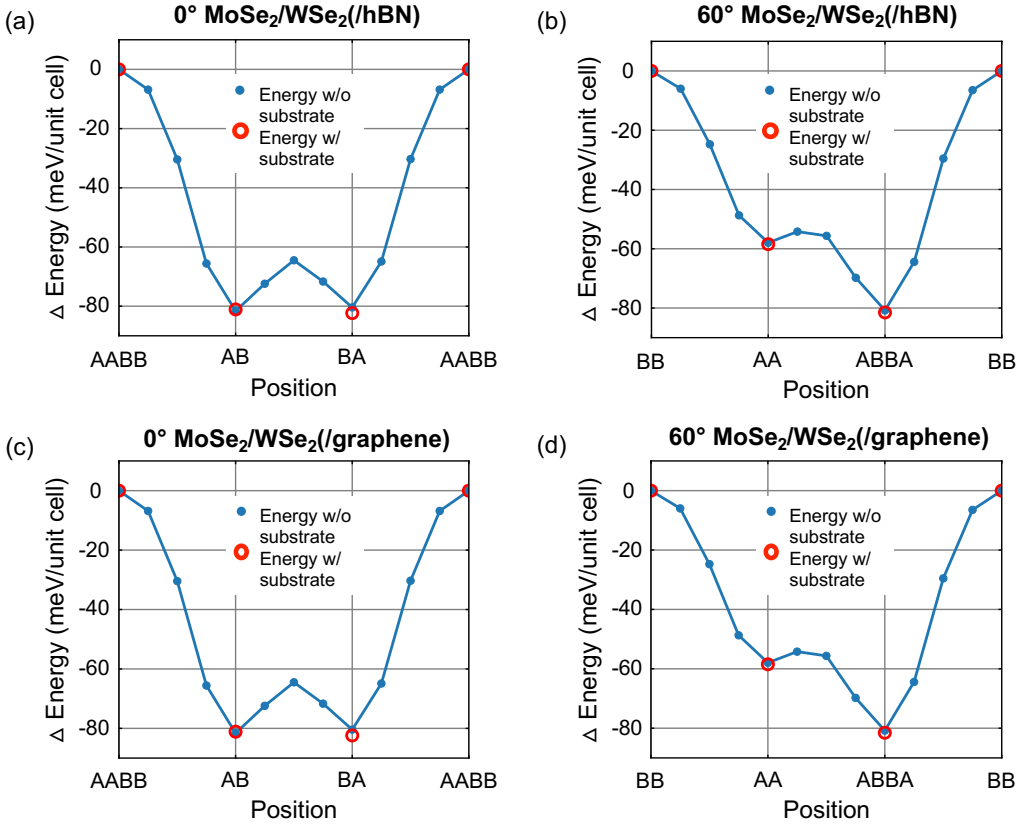

Figure S13. Impact of substrate on stacking energy calculations. (a) Stacking energy as a function of stacking orientation (similar to Fig. 1(b), Fig. 1(e), and Fig. S3) for the (a) 0° aligned $WSe_2/MoSe_2$ stack and (b) 60° aligned $WSe_2/MoSe_2$ stack. The blue filled circles represent calculations without a substrate. The red open circles are the calculations including 1 layer of hBN included beneath WSe_2. (c-d) Similar plots to (a) and (b) except the red circles correspond to calculations with 1 layer of graphene included beneath WSe_2. The angle of the graphene and hBN relative to the WSe_2 was 19.1° (4 unit cells of $MoSe_2/WSe_2$ on top of 7 unit cells of graphene or hBN) with less than 1% strain in the substrate.